

Excitons in Magnetic Fields

Kankan Cong, G Timothy Noe II, and Junichiro Kono, Rice University, Houston, TX, United States

© 2018 Elsevier Ltd. All rights reserved.

Introduction

When a photon of energy greater than the band gap is absorbed by a semiconductor, a negatively charged electron is excited from the valence band into the conduction band, leaving behind a positively charged hole. The electron can be attracted to the hole via the Coulomb interaction, lowering the energy of the electron-hole (e - h) pair by a characteristic binding energy, E_b . The bound e - h pair is referred to as an exciton, and it is analogous to the hydrogen atom, but with a larger Bohr radius and a smaller binding energy, ranging from 1 to 100 meV, due to the small reduced mass of the exciton and screening of the Coulomb interaction by the dielectric environment.

Like the hydrogen atom, there exists a series of excitonic bound states, which modify the near-band-edge optical response of semiconductors, especially when the binding energy is greater than the thermal energy and any relevant scattering rates. When the e - h pair has an energy greater than the binding energy, the electron and hole are no longer bound to one another (ionized), although they are still correlated. The nature of the optical transitions for both excitons and unbound e - h pairs depends on the dimensionality of the e - h system. Furthermore, an exciton is a composite boson having integer spin that obeys Bose-Einstein statistics rather than fermions that obey Fermi-Dirac statistics as in the case of either the electrons or holes by themselves. One of the most interesting consequences of the bosonic nature of excitons is the possibility of having many that occupy the same quantum state as opposed to fermions, which obey the Pauli exclusion principle.

An applied magnetic field, \vec{B} , will quantize the energies and angular momenta of charged particles and thus change the electronic state of an exciton. In general, the excitonic wavefunction shrinks in the direction perpendicular to \vec{B} , and the exciton binding energy increases with $B = |\vec{B}|$. How the energy of each exciton state varies with B depends on basic exciton parameters, and, therefore, the study of excitons in B provides a tool to characterize various exciton properties, such as the reduced mass, binding energy, Bohr radius, and g -factor. Importantly, the nature of the dependence of exciton energy on B depends on the strength of B . For example, at low B , where the effect of the Coulomb interaction is larger than that of B and thus B is treated as a perturbation, excitons retain a hydrogenic nature: diamagnetic shifts and Zeeman splittings modify the energies of excitonic states. Alternatively, in the high B limit where the effect of B dominates and the Coulomb interaction is treated as a perturbation, the energies of exciton states show Landau-level-like, linear- B dependence, similar to free e - h pairs.

For the hydrogen atom, the binding energy, 13.6 eV, is much higher than those for excitons in semiconductors, and an extremely high B (over 2×10^5 T) is required to enter the high B regime. The much smaller binding energies of excitons in semiconductors allow one to enter the high- B regime readily, which, together with the bosonic nature of excitons, makes excitons in high B attractive for the investigation of many-body phenomena in condensed matter in a highly controllable manner. A large body of theoretical work has thus been devoted in the last several decades to e - h systems in strong B , and a fascinating array of possible physical phenomena/states has been predicted – the excitonic insulator phase, a gas-liquid-type phase transition, Bose-Einstein condensation of magnetoexcitons, and quantum chaos. Recently, attention has been paid to spatially separated two-dimensional (2D) electrons and holes in layered structures, since the pioneering work of Lozovik and co-workers, who considered the pairing of electrons and holes across an interface of two-media, and the superfluidity of such pairs. A very interesting but complicated many-particle situation arises, in the presence of strong perpendicular B . In such a situation, spatially separated 2D electrons and holes, both Landau quantized, are present, and there is a Coulomb attraction between them as well as electron-electron (e - e) and hole-hole (h - h) correlations. However, all these interactions are expected to cancel each other in the high- B limit, where the “hidden symmetry” of 2D magnetoexcitons protects them from ionization, leading to the absence of an excitonic Mott transition. Furthermore, excitonic gain enhancement occurs in a high-density e - h system in high B , which leads to cooperative and coherent light emission (known as superfluorescence) from the highest-occupied magnetoexciton state.

Here, we will review various observations related to excitons in magnetic fields. First, we present the theory of excitons in magnetic fields and show how the exciton energy's magnetic field dependence relates to fundamental exciton parameters. We will explore how different dimensionalities of excitons and the strength of magnetic fields affect the exciton properties. Then, interband and intraband magneto-optical absorption observations are discussed in different semiconductor systems. Finally, some exotic phenomena unique to high-density excitons in high magnetic fields are presented.

Exciton States in Magnetic Fields

In this section, we describe the states of excitons in semiconductors in different dimensions and B regimes. We introduce the basic Hamiltonians of excitons, discuss the eigenenergies in the low- B and high- B limits, and define some basic parameters of excitons and various quantities to be used throughout the article.

For an electron with effective mass m_e^* located at \vec{r}_e and a hole with effective mass m_h^* located at \vec{r}_h , interacting through the Coulomb potential $U(\vec{r}) = \frac{e^2}{4\pi\epsilon r}$, the Hamiltonian at zero B is given by

$$\hat{H} = -\frac{\hbar^2}{2M^*} \nabla_R^2 - \frac{\hbar^2}{2\mu^*} \nabla_r^2 + U(\vec{r}) \quad (1)$$

where $M^* = m_e^* + m_h^*$ is the total mass, $\mu^* = ((m_e^*)^{-1} + (m_h^*)^{-1})^{-1}$ is the reduced mass, the center-of-mass coordinate $\vec{R} = (m_e^* \vec{r}_e + m_h^* \vec{r}_h)/M^*$, the relative coordinate $\vec{r} = \vec{r}_e - \vec{r}_h$, ∇_R^2 (∇_r^2) is the Laplacian expressed in the center-of-mass (relative) coordinates, \hbar is the reduced Planck constant, e is the electronic charge, $\epsilon = \epsilon_r \epsilon_0$ is the permittivity, ϵ_r is the relative permittivity (dielectric constant), and ϵ_0 is the vacuum permittivity.

Three-Dimensional Case

In a three-dimensional (3D) system at zero B , the Schrödinger equation for the relative motion is given by

$$\left(-\frac{\hbar^2}{2\mu^*} \nabla_r^2 - \frac{e^2}{4\pi\epsilon r} \right) \psi(\vec{r}) = E \psi(\vec{r}) \quad (2)$$

where $\Psi(\vec{r})$ is the exciton wavefunction and E is the energy of the exciton. In spherical coordinates, the wavefunction can be expressed as $\Psi(r, \theta, \phi) = R_{nl}(r) Y_{lm}(\theta, \phi)$, where $R_{nl}(r)$ and $Y_{lm}(\theta, \phi)$ are the radial and angular wavefunctions, respectively, n ($= 1, 2, 3, \dots$) is the principal quantum number, l ($= 0, 1, 2, \dots, n-1$) is the azimuthal quantum number, and m ($= 0, \pm 1, \dots, \pm l$) is the magnetic quantum number. The eigenenergies are

$$E_n = -\frac{R_y^*}{n^2}, \quad n = 1, 2, 3, \dots \quad (3)$$

where R_y^* is the effective Rydberg constant defined as

$$R_y^* = \frac{\mu^* e^4}{32\pi^2 \epsilon^2 \hbar^2} = \frac{\mu^* / m_e}{\epsilon_r^2} \times 13.6 \text{ eV} \quad (4)$$

where $m_e = 9.11 \times 10^{-31} \text{ kg}$ is the mass of a free electron in vacuum. Therefore, the binding (ionization) energy of a 3D exciton is $E_{b,3D}^* = E_\infty - E_1 = R_y^*$. Using the effective Bohr radius

$$a_{B,3D}^* = \frac{4\pi\epsilon\hbar^2}{\mu^* e^2} = \frac{\epsilon_r}{\mu^* / m_e} \times 0.0529 \text{ nm} \quad (5)$$

the binding energy can be expressed as

$$E_{b,3D}^* = \frac{\hbar^2}{2\mu^*} \frac{1}{(a_{B,3D}^*)^2} \quad (6)$$

and the 1s state wavefunction is given by

$$\Psi_{1s,3D} = \Psi_{100} = \frac{1}{\sqrt{\pi}} \frac{1}{(a_{B,3D}^*)^{3/2}} \exp\left(\frac{-r}{a_{B,3D}^*}\right) \quad (7)$$

Now that we have defined the basic quantities for excitons, let us consider the effect of a uniform and constant magnetic field, $\vec{B} = (0, 0, B)$. The excitonic eigenenergies and wavefunctions are modified through the inclusion of vector potential \vec{A} in the Hamiltonian, for which $\vec{B} = \nabla \times \vec{A}$. The Hamiltonian of the system becomes (neglecting electron spin)

$$\begin{aligned} \hat{H} &= \frac{1}{2m_e^*} \left(\vec{p}_e + e\vec{A}(\vec{r}_e) \right)^2 + \frac{1}{2m_h^*} \left(\vec{p}_h - e\vec{A}(\vec{r}_h) \right)^2 - \frac{e^2}{4\pi\epsilon r} \\ &= -\frac{\hbar^2}{2m_e^*} \nabla_e^2 - \frac{\hbar^2}{2m_h^*} \nabla_h^2 - \frac{e^2}{4\pi\epsilon r} - \frac{ie\hbar}{m_e^*} \vec{A}(\vec{r}_e) \cdot \vec{\nabla}_e \\ &\quad + \frac{ie\hbar}{m_h^*} \vec{A}(\vec{r}_h) \cdot \vec{\nabla}_h + \frac{e^2}{2m_e^*} A^2(\vec{r}_e) + \frac{e^2}{2m_h^*} A^2(\vec{r}_h) \end{aligned} \quad (8)$$

where \vec{p}_e and \vec{p}_h are the momentum operators of the electron and hole, respectively.

Following Gor'kov and Dzyaloshinskii, we use a canonical transformation to obtain a new wavefunction $\Psi'(\vec{R}, \vec{r})$

$$\Psi'(\vec{R}, \vec{r}) = \exp\left(i\left[\vec{K} - \frac{e}{\hbar} \vec{A}(\vec{r})\right] \cdot \vec{R}\right) F(\vec{r}) \quad (9)$$

where $F(\vec{r})$ is an arbitrary function of \vec{r} , and $\vec{K} = \vec{k}_e - \vec{k}_h$. After the transformation, the Schrödinger equation becomes

$$\hat{H}' F(\vec{r}) = \left[E - \frac{\hbar^2 K^2}{2M^*} \right] F(\vec{r}) \quad (10)$$

with the new Hamiltonian expressed as

$$\begin{aligned}\hat{H}' &= \left(-\frac{\hbar^2}{2\mu^*} \nabla_r^2 - \frac{e^2}{4\pi\epsilon r} \right) - ie\hbar \left(\frac{1}{m_e^*} - \frac{1}{m_h^*} \right) \vec{A}(\vec{r}) \cdot \vec{\nabla}_r \\ &\quad + \frac{e^2}{2\mu^*} A^2(\vec{r}) - \frac{2e\hbar}{M^*} \vec{A}(\vec{r}) \cdot \vec{K} \\ &= \hat{H}_{B=0} + \frac{\omega_{c,e} - \omega_{c,h}}{2} \hat{L}_z + \frac{e^2 B^2}{8\mu^*} (x^2 + y^2) \\ &\quad - \frac{eB\hbar}{M^*} (xK_y - yK_x)\end{aligned}\quad (11)$$

$$- \frac{eB\hbar}{M^*} (xK_y - yK_x) \quad (12)$$

where $\omega_{c,i} = eB/m_i^*$ ($i=e,h$) is the cyclotron frequency, $\hat{L}_z = -i\hbar \left(x \frac{\partial}{\partial y} - y \frac{\partial}{\partial x} \right)$ is the z -component of the orbital angular momentum operator, and the symmetric gauge, $\vec{A} = (1/2)(-By, Bx, 0)$, was used in the final step. The first term of \hat{H}' is the Hamiltonian at zero B . The second term is referred to as the (orbital) Zeeman term, which leads to shifts and splittings of exciton states, depending on the value and degeneracy of the orbital angular momentum of a given state. The third term is the Langevin diamagnetism term, which is proportional to the spatial extent of the exciton wavefunction in a plane perpendicular to \vec{B} and increases quadratically with increasing B . The fourth term can be rewritten as $-e(\vec{V}_R \times \vec{B}) \cdot \vec{r}$, where \vec{V}_R is the center-of-mass velocity. Since \vec{r} is the relative coordinate, the fourth term implies that the relative and center-of-mass degrees of freedom are coupled in the presence of a B .

It should be pointed out that one cannot obtain an exact solution to the Schrödinger equation corresponding to Eq. (11), which is related to quantum chaos. This is due to the fact that the number of conserved quantities (two), i.e., E and L_z , is smaller than the number of degrees of freedom (three), a situation known to be *non-integrable*, for which the classical trajectories of energy states in phase space are chaotic. Correspondingly, energy levels exhibit fluctuations; with increasing energy, the statistics of levels evolve from Poissonian to Gaussian. Approximate solutions can be obtained only for low-energy levels either in the low- B limit or the high- B limit, and a one-to-one correspondence of states between these two limits does not exist, in general, because of the different symmetries the magnetic field and the Coulomb potential possess: the cylindrical symmetry (for the former) and the spherical symmetry (for the latter).

To define the low- B and high- B limits, we introduce a dimensionless parameter

$$\gamma \doteq \frac{\hbar\omega_c}{2}/R_\gamma^* = \left(\frac{a_B^*}{l_B} \right)^2 = \frac{16\pi^2 \hbar^3 e^2}{\mu^{*2} e^3} B \quad (13)$$

where $l_B = \sqrt{\hbar/eB}$ is the magnetic length and $\omega_c = eB/\mu^*$ is the reduced cyclotron frequency. The value of γ is a measure of whether the energy of the exciton is dominated by the influence of the magnetic field or the Coulomb interaction. In the low- B limit ($\gamma \ll 1$), the system is nearly hydrogenic, and the Zeeman and diamagnetic terms can be treated as a perturbation in Eq. (11). (Note that the fourth term in \hat{H}' is usually negligible because of the smallness of K relevant to optical transitions.) For the $1s$ [or $(n,l,m)=(100)$] state, $\langle L_z \rangle = m\hbar = 0$, and therefore, the Zeeman term is zero, and the first-order correction is the diamagnetic term:

$$\begin{aligned}\Delta E_{1s,3D} &= \left\langle \frac{e^2 B^2}{8\mu^*} (x^2 + y^2) \right\rangle_{1s,3D} \\ &= \frac{e^2 B^2}{8\mu^*} \langle \Psi_{1s,3D} | (x^2 + y^2) | \Psi_{1s,3D} \rangle \\ &= \frac{e^2 B^2}{8\mu^*} \cdot 2 \left(a_{B,3D}^* \right)^2 = \sigma_{3D}^* B^2\end{aligned}\quad (14)$$

$$\sigma_{3D}^* \doteq \frac{e^2}{4\mu^*} \left(a_{B,3D}^* \right)^2 = \frac{4\pi^2 e^2 \hbar^4}{e^2 (\mu^*)^3} \quad (15)$$

Here, σ_{3D}^* is the 3D diamagnetic-shift coefficient, which depends on μ^* and $a_{B,3D}^*$. This fact offers a straightforward experimental method for determining $a_{B,3D}^*$ (or, more generally, the spatial extent of the exciton wavefunction) once the reduced mass is known. In addition, measuring σ_{3D}^* as the direction of \vec{B} is varied allows one to map out the wavefunction anisotropy. Similarly, the diamagnetic shift for the ns exciton state can be calculated to be

$$\Delta E_{ns,3D} = \frac{n^2(5n^2 + 1)}{6} \sigma_{3D}^* B^2 \quad (16)$$

For calculating the energy for a p -like state, one must include the Zeeman term. For example, the $2p$ state splits into three states in a B with $\langle L_z \rangle = 0, \pm 1$, so the orbital Zeeman energy is

$$\Delta E_{\text{Zeeman}} = 0, \pm \frac{\hbar\omega_c}{2} \quad (17)$$

In the high- B limit ($\gamma \gg 1$), where the effect of the magnetic field is much larger than the Coulomb interaction, the Coulomb interaction is treated as a small perturbation. Under this condition, the energies and wavefunctions of excitons can be separated into different components for the x - y plane and the z -direction (known as the 'adiabatic' approximation). In the x - y plane, only the effect of the magnetic field has to be considered, while in the z -direction, only the Coulomb interaction contributes, because a magnetic field applied in the z -direction exerts a Lorentz force only in the x - y plane. The wavefunction can then be expressed as

$$\Psi_{NMi} = \Phi_{NM}(x, y) f_{NMi}(z) \quad (18)$$

where $N=0, 1, 2, \dots$ is the Landau quantum number, $M=N, N-1, \dots, -\infty$ is the azimuthal quantum number, and $i=0, 1, 2, \dots$ is the quantum number associated with the motion in the z -direction. The wavefunction $\Phi_{NM}(x, y)$ describes the in-plane motion and is proportional to the associated Laguerre function $L_{N+|M|}^{|M|}$.

The total energy is characterized by three quantum numbers (N, M, v^+) for $i=2v$ ($v=0, 1, 2, \dots$), and (N, M, v^-) for $i=2v-1$ ($v=1, 2, \dots$):

$$E_{NM(v)} = \left(N + \frac{1}{2}\right) \hbar \omega_c + \Delta E_{NMv}(z) \quad (19)$$

Hence, in the high- B limit, the states become more Landau-level-like, exhibiting a linear B dependence (the first term) with the Coulombic correction, $\Delta E_{NMv}(z)$, which is a red-shift for each eigenenergy at a fixed value of z . The wavefunction $f_{NMv^+}(z)$ is an even function, while $f_{NMv^-}(z)$ is an odd function with respect to z .

Because of the reason stated earlier, there is no general correspondence between the low-field notation (n, l, m) and high-field notation (N, M, v) for a 3D exciton. However, using the principle of conservation of the number of nodal surfaces, Shinada *et al.* made the following correspondence for the lowest-lying exciton states:

$$\begin{aligned} 1s &\leftrightarrow (0, 0, 0^+) \\ 2s &\leftrightarrow (0, 0, 1^+) \\ 2p_0 &\leftrightarrow (0, 0, 1^-) \\ 2p_+ &\leftrightarrow (1, 1, 0^+) \\ 2p_- &\leftrightarrow (0, -1, 0^+) \\ 3d_0 &\leftrightarrow (1, 0, 0^+) \end{aligned} \quad (20)$$

Two-Dimensional Case

For 2D excitons, we use a polar coordinate system,

$$\vec{\rho} = (x, y) = (\rho \cos \phi, \rho \sin \phi) \quad (21)$$

At zero B , the Hamiltonian for the relative motion for a 2D e - h pair is written as

$$\begin{aligned} \hat{H} &= -\frac{\hbar^2}{2\mu^*} \left(\frac{\partial^2}{\partial x^2} + \frac{\partial^2}{\partial y^2} \right) - \frac{e^2}{4\pi\epsilon \sqrt{x^2 + y^2}} \\ &= -\frac{\hbar^2}{2\mu^*} \left(\frac{\partial^2}{\partial \rho^2} + \frac{1}{\rho} \frac{\partial}{\partial \rho} + \frac{1}{\rho^2} \frac{\partial^2}{\partial \phi^2} \right) - \frac{e^2}{4\pi\epsilon \rho} \end{aligned} \quad (22)$$

By solving the Schrödinger equation

$$\hat{H}\Psi(\rho, \phi) = E\Psi(\rho, \phi) \quad (23)$$

we obtain the eigenenergies as

$$E_n = \frac{\mu^* e^4}{32\pi^2 \epsilon^2 \hbar^2 (n - \frac{1}{2})^2} = -\frac{R_y^*}{(n - \frac{1}{2})^2}, \quad n = 1, 2, 3, \dots \quad (24)$$

The binding energy is then calculated to be

$$E_{b,2D}^* = E_\infty - E_1 = 4R_y^* = 4E_{b,3D}^* \quad (25)$$

which is four times larger than that of the 3D case for the same semiconductor. The eigenstates have the form

$$\Psi_{nm} = R_{nm}(\rho) e^{im\phi}$$

where $n (= 1, 2, 3, \dots)$ is the principal quantum number, and $m (= -n+1, \dots, -2, -1, 0, 1, 2, \dots, n-1 = \dots, d_-, p_-, s, p_+, d_+, \dots)$ is the angular momentum quantum number. The $1s$ exciton wavefunction is written as

$$\Psi_{1s,2D} = \Psi_{10} = R_{10} = \frac{1}{\sqrt{2\pi}} \frac{2}{a_{B,2D}^*} \exp\left(\frac{-\rho}{a_{B,2D}^*}\right) \quad (26)$$

with the effective Bohr radius,

$$a_{B,2D}^* = \frac{2\pi\epsilon\hbar^2}{\mu^*e^2} = \frac{a_{B,3D}^*}{2} \quad (27)$$

which is only half of that of a 3D exciton in the same semiconductor material. From Eqs. (4), (25) and (27), we have

$$E_{b,2D}^* = \frac{\hbar^2}{2\mu^*} \frac{1}{(a_{B,2D}^*)^2} \quad (28)$$

In a similar manner to the 3D case, the Hamiltonian of the 2D system at a finite B after the Gor'kov-Dzyaloshinskii transformation can be written as

$$\begin{aligned} \hat{H}' = & \left(-\frac{\hbar^2}{2\mu^*} \nabla_\rho^2 - \frac{e^2}{4\pi\epsilon\rho} \right) - ie\hbar \left(\frac{1}{m_e^*} - \frac{1}{m_h^*} \right) \vec{A}(\vec{\rho}) \cdot \vec{\nabla}_\rho \\ & + \frac{e^2}{2\mu^*} A^2(\vec{\rho}) - \frac{2e\hbar}{M} \vec{A}(\vec{\rho}) \cdot \vec{K} \end{aligned} \quad (29)$$

$$\begin{aligned} = & \hat{H}_{B=0} + \frac{\omega_{c,e} - \omega_{c,h}}{2} \hat{L}_z + \frac{e^2 B^2}{8\mu^*} (x^2 + y^2) \\ & - \frac{eB\hbar}{M} (xK_y - yK_x) \end{aligned} \quad (30)$$

where the symmetric gauge is used. Also, similar to the 3D case, the diamagnetic shift for the $1s$ state can be calculated to be

$$\begin{aligned} \Delta E_{1s,2D} &= \frac{e^2 B^2}{8\mu^*} \langle \rho^2 \rangle_{1s,2D} = \frac{e^2 B^2}{8\mu^*} \frac{3}{8} (a_{B,3D}^*)^2 \\ &= \sigma_{2D}^* B^2 \end{aligned} \quad (31)$$

$$\begin{aligned} \sigma_{2D}^* &= \frac{3e^2}{64\mu^*} (a_{B,3D}^*)^2 = \frac{3e^2}{16\mu^*} (a_{B,2D}^*)^2 \\ &= \frac{3\pi^2 \epsilon^3 \hbar^4}{4e^2 (\mu^*)^3} = \frac{3}{16} \sigma_{3D}^* \end{aligned} \quad (32)$$

$$a_{B,2D}^* = \sqrt{\langle \rho^2 \rangle_{1s,2D}} = \sqrt{8\mu^* \sigma_{2D}^*} / e \quad (33)$$

Here, σ_{2D}^* is the 2D diamagnetic-shift coefficient, and $a_{B,2D}^*$ is equal to the root mean squared (r.m.s.) radius of the $1s$ exciton. So, the diamagnetic-shift coefficient of a 2D exciton is much smaller than the corresponding 3D excitons in the same semiconductor material, i.e., a larger Coulomb interaction makes the wavefunction more compact, leading to a smaller diamagnetic shift.

In a 2D system, both the B and the Coulomb energy have circular symmetry, and thus, there is a straightforward, one-to-one correspondence between the low- B notation (n,m) and the high- B notation (N,M) , as summarized in Table 1. The correspondence rules are:

$$m = N - M \quad (34)$$

$$n = N + 1 \text{ (for } N \geq M) \quad (35)$$

$$n = M + 1 \text{ (for } M \geq N) \quad (36)$$

Here, n and m are the principle and angular momentum quantum numbers, respectively, in the low- B hydrogenic notation, while M and N are the Landau indices of the electron and hole, respectively, in the high- B Landau-level notation. For example, if $N=0$ and $M=0$, we get $n=1$ and $m=0$, i.e., $(N,M)=(0,0)$ corresponds to the $1s$ state. Also, if $N=3$ and $M=2$, we obtain $n=4$ and $m=+1$, and so $(N,M)=(3,2)$ corresponds to the $4p^+$ state.

Table 1 Correspondence between the low- and high- B labels $(n,m) \leftrightarrow (N,M)$ for 2D magnetoexcitons, where $m=N-M$ and $n=N+1$ for $N \geq M$ and $n=M+1$ for $M \geq N$

M	0	1	2	3
N				
0	$1s$	$2p^-$	$3d^-$	$4f^-$
1	$2p^+$	$2s$	$3p^-$	$4d^-$
2	$3d^+$	$3p^+$	$3s$	$4p^-$
3	$4f^+$	$4d^+$	$4p^+$	$4s$

Source: Reproduced (adapted) with permission from MacDonald, A.H., Ritchie, D.S., 1986. Hydrogenic energy levels in two dimensions at arbitrary magnetic fields. Physical Review B 33, 8336–8344. Copyright 1986 by the American Physical Society.

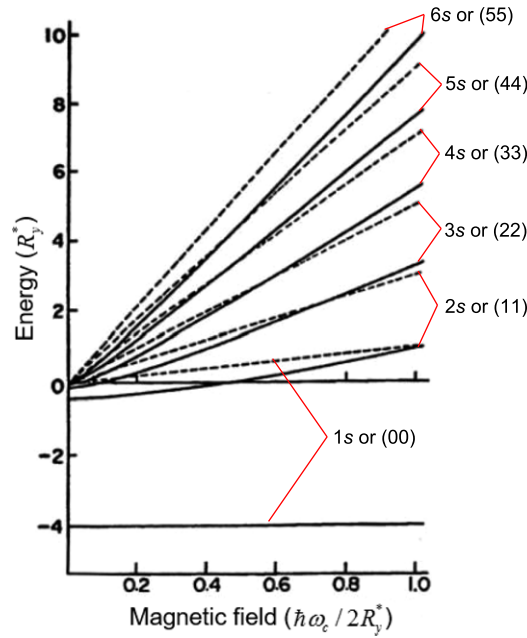


Fig. 1 (color online). Calculated eigenenergies of 2D excitons as a function of dimensionless magnetic field, $\gamma = \hbar\omega_c/2R_y^*$, with (solid lines) and without (dashed lines) the Coulomb interaction. Reproduced (adapted) with permission from Akimoto, O., Hasegawa, H., 1967. Interband optical transitions in extremely anisotropic semiconductors. II. Coexistence of exciton and the Landau levels. Journal of the Physical Society of Japan 22, 181–191. Copyright 1967 by the Physical Society of Japan.

Fig. 1 plots the eigenenergies of the lowest six 2D exciton states as a function of dimensionless magnetic field γ , calculated by Akimoto and Hasegawa. The solid and dashed lines represent the energies of the exciton states with and without including the Coulomb interaction in the Hamiltonian, respectively. At low B , the excitonic feature dominates the low-index energy states. The high-index energy states and the states at high fields show a more Landau-level-like behavior, more appropriate for free electrons and holes. The lowest-energy state or the 1s [or the (00)] state remains constant with increasing γ up to ~ 1 , but in the higher γ range it curves upward to cross the $E=0$ line and eventually runs parallel to the linear Landau level line at $\gamma \sim 12.5$.

Interband Magneto-optical Absorption

Interband magneto-optical absorption can provide direct information on the energy levels of optically accessible (or ‘bright’) exciton states: ns states (1s, 2s, 3s, ...) in the low- B notation, or $(N,M)=(00), (11), (22), \dots$ states in the high- B notation. To be clear, these are simply notations, and there is a one-to-one correspondence between the two (see **Table 1**). In the low- B limit, the 1s energy state shows a hydrogenic character with the energy quadratically dependent on B . The effective diamagnetic-shift coefficient, σ^* , can be determined from the B^2 fitting of the exciton energy. If the reduced mass of excitons is known, the Bohr radius can be obtained from **Eq. (33)**. In addition, the binding energy can be determined using **Eq. (28)**, assuming that a hydrogenic model applies to the semiconductor under study. The reduced effective mass can be obtained from the cyclotron frequency $\omega_c = eB/\mu^*$, which is deduced from the slope versus B of exciton energies in the high- B limit. Furthermore, by extrapolating the B -dependent energy lines of excited exciton states in the high- B limit to the zero- B value, it is found that they nearly converge to a single point, which gives the band gap. The difference between the band gap and the 1s exciton peak at zero B then gives the exciton binding energy.

Quantum Wells

The first magneto-optical absorption experiment in a semiconductor quantum well system was performed by Tarucha *et al.* in 1984. They used undoped GaAs/AlAs multiple-quantum wells grown on a (100) GaAs substrate by molecular beam epitaxy. Optical absorption spectra were taken at 4.2 K in pulsed B up to 30 T applied perpendicular to the sample. **Fig. 2(a)** shows absorption spectra at different B . At 0 T, the absorption spectrum shows two distinct peaks, corresponding to the 1s heavy-hole ($E_{hh}(1s)$) and 1s light-hole ($E_{lh}(1s)$) excitons, respectively. With increasing B , the 1s exciton peaks were observed to blue-shift, and additional peaks emerged at higher energies, corresponding to the ns states (2s, 3s, ...) in the low- B notation, or $(N,M)=(11), (22), \dots$ states in the high- B notation. These higher-energy peaks blue-shifted more rapidly with increasing B .

Fig. 2(b) shows the photon energies of the absorption peaks as a function of B . The 1s heavy-hole and light-hole excitons are represented by solid and open circles, respectively, and the peaks of higher energy states are plotted with crosses. In the low- B

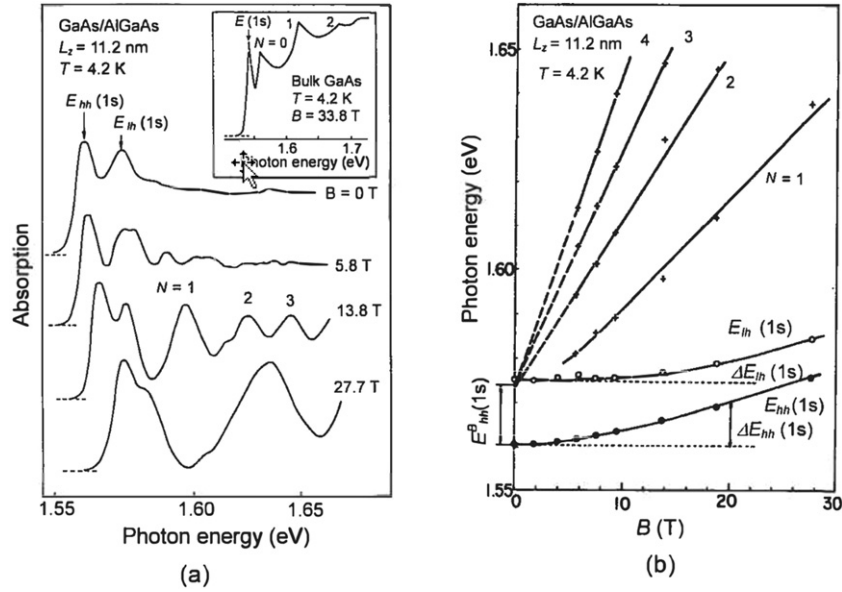


Fig. 2 (color online). (a) Optical absorption spectra at different magnetic fields for a GaAs/AlGaAs multiple-quantum-well sample. (b) Magnetic field dependence of the photon energies of absorption peaks. Reproduced (adapted) with permission from Tarucha, S., Okamoto, H., Iwasa, Y., Miura, N., 1984. Exciton binding energy in GaAs quantum wells deduced from magneto-optical absorption measurement. Solid State Communications 52, 815–819. Copyright 1984 by Elsevier.

region, the $1s$ exciton energy shows a quadratic field dependence, in agreement with the expected diamagnetic shift in energy for excitons. In addition, the change of the heavy-hole transition energy at a certain field $\Delta E_{hh}(1s)$ is observed to be larger than the change of the light-hole transition energy $\Delta E_{lh}(1s)$ at the same field, indicating a smaller reduced mass for the $1s$ heavy-hole excitons than that of the $1s$ light-hole excitons, since the diamagnetic shift is proportional to $1/\mu^*$; see Eq. (31). The difference in the reduced masses of excitons can be explained by the anisotropic nature of the kinetic energy expression in the diagonal term of the Luttinger-Kohn Hamiltonian. The diagonal term gives the larger reduced mass for the light-hole excitons associated with $J_z(\pm 3/2)$ bands than that for the heavy-hole excitons associated with $J_z(\pm 1/2)$ bands.

In contrast, the absorption peaks for higher-energy heavy-hole states show a linear B dependence. The effect of the Coulomb interaction can only be seen on the $2s$ state, since its energy shift shows a small curvature in the low- B region. By extrapolating the $3s$, $4s$, and $5s$ absorption peaks from the high- B region to the low- B region with straight lines, it was found that the lines converge at a photon energy within an error of less than 0.5 meV. The difference between the energy at the convergent point and the zero field value of $E_{hh}(1s)$ gives the binding energy of the $1s$ heavy-hole exciton, which was ~ 15 meV in this case. The exciton binding energy of the $1s$ heavy-hole exciton increases with decreasing well size, since the quasi-2D nature is a closer approximation for smaller quantum well sizes. On the contrary, the diamagnetic shift increases with increasing well size, indicating a larger Bohr radius in a higher-dimensionality system.

Transition Metal Dichalcogenide

Atomically thin transition-metal dichalcogenides (TMDs), a new class of 2D materials, have recently attracted much attention for magneto-optical studies due to their extremely large exciton binding energies. For example, Stier *et al.* performed low-temperature polarized reflection measurements on atomically thin WS_2 and MoS_2 in high magnetic fields up to 65 T, observing a strong Zeeman splitting and a small diamagnetic shift for the 2D excitons. Based on their measurements, some basic parameters of excitons in these TMDs, such as the g -factor, exciton size, and binding energy, were determined.

As shown in Fig. 3(a), 2D TMDs have a direct band gap located at the degenerate K and K' valleys of their hexagonal Brillouin zones. The strong spin-orbit coupling of the valence band lifts the degeneracy of the spin-up and spin-down components, leading to well-separated A and B excitons. Due to the valley-specific optical selection rules, the interband transitions in the K valley only couple to right circularly polarized light, σ^+ , for both the A and B excitons, but left circularly polarized light, σ^- , for the K' valley.

Fig. 3(b) plots the B -dependent energy shifts of the conduction and valence bands in the K valley (σ^+ polarized light) with $B \parallel \pm z$, and demonstrates different contributions to the Zeeman splitting. For a specific valley in a B , the Zeeman shift is $\Delta E_Z = -(\mu_c - \mu_v) \cdot B$. In addition, the time-reversal symmetry in TMDs leads to an equal-but-opposite total magnetic moment ($\mu_K^{c,v} = -\mu_{K'}^{c,v}$) in the K and K' valleys. However, this time-reversal symmetry will be broken by B , and the time-reversed pairs in K and K' valleys will shift to opposite directions, i.e., the Zeeman splitting for excitons is doubled considering the broken time-reversal symmetry. Generally, the total magnetic moment μ comes from three sources: spin (μ_s), atomic orbital (μ_l), and valley

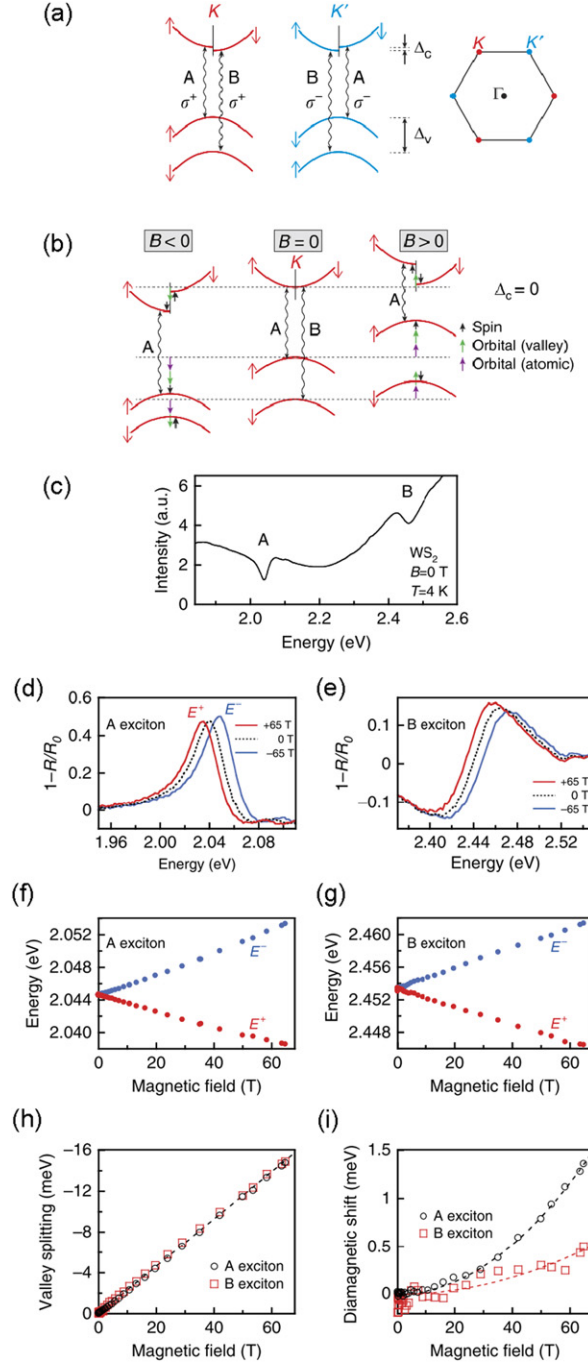


Fig. 3 (color online). (a) Excitonic transitions in monolayer transition metal dichalcogenides. (b) Zeeman shifts in different B fields. (c) Reflection spectra of monolayer WS_2 at $B=0$ T and $T=4$ K. (d) Normalized reflection spectra of the A exciton resonance in different B . (e) Same, but for the B exciton. (f) Energy of the field-split A exciton versus magnetic field. (g) Same, but for the B exciton. (h) The measured valley Zeeman splitting versus B , for both the A and B excitons. (i) The diamagnetic shifts for both the A and B excitons. Reproduced (adapted) with permission from Stier, A.V., McCreary, K.M., Jonker, B.T., Kono, J., Crooker, S., 2016. Exciton diamagnetic shifts and valley Zeeman effects in monolayer WS_2 and MoS_2 to 65 Tesla. *Nature Communications* 7, 10643. Copyright 2016 by Nature Publishing Group.

orbital (μ_k) (Berry curvature). Here, μ_s is zero, since the optically allowed transitions couple the conduction and valence bands with the same spin. μ_l is non-zero, since the conduction and valence bands have different atomic orbitals. The d_{z^2} orbitals of the conduction band have $L_z=0$ ($\mu_l^c=0$), while the hybridized $d_{x^2-y^2} \pm id_{xy}$ orbitals for the valence bands have $L_z=\pm 2\hbar$ ($\mu_l^v=\pm 2\mu_B$) in the K and K' valleys, generating a Zeeman shift of $\mp 2\mu_B B$ for the K and K' excitons, and leading to a total exciton splitting of $-4\mu_B B$. For the valley orbital contribution to the conduction and valence bands, $\mu_k^c=\pm(m_e/m_e^*)\mu_B$ and $\mu_k^v=\pm(m_e/m_h^*)\mu_B$ in the K and K' valleys. Assuming a simple two-band tight-binding model where $m_e^*=m_h^*$, it is easy to see that $\mu_k^c=\mu_k^v$, i.e., the

contribution of the valley orbital to the Zeeman splitting is zero. In total, the Zeeman splitting for excitons is expected to be $\Delta E_Z = -4\mu_B B$ assuming $m_e^* = m_h^*$.

Fig. 3(c) shows the reflection spectrum of monolayer WS_2 at 4 K and 0 T, from which the A and B excitonic transitions can be seen. The normalized reflection spectra at 0 T and ± 65 T of the A exciton are shown in **Fig. 3(d)**, indicating a clear Zeeman splitting of ~ 15 meV. The valley splitting of the B exciton can also be observed, as shown in **Fig. 3(e)**. For both excitons, the exciton transition energy in a positive B (called E^+) shifts to a lower energy, while a shift to a higher energy is observed for the exciton transition energy in a negative B (called E^-). **Fig. 3(f)** and **(g)** show the transition energies, E^+ and E^- , as a function of B , for the A and B excitons, respectively. The splittings between the two valleys, $E^+ - E^-$, are shown in **Fig. 3(h)** for both the A and B excitons. The measured Zeeman splitting energies are negative but increase linearly with B with almost identical rates of $-228 \pm 2 \mu\text{eV T}^{-1}$ for the A exciton and $-231 \pm 2 \mu\text{eV T}^{-1}$ for the B exciton. Such rates correspond to g -factors of -3.94 ± 0.04 and -3.99 ± 0.04 , respectively, very close to the expected value (-4).

Fig. 3(i) shows the diamagnetic shifts for the A and B excitons in monolayer WS_2 . As we saw in Eq. (33), $a_{B,2D}^*$ can be calculated if μ^* and σ_{2D}^* are known.

Through fits to the data, $\sigma_A^* = 0.32 \pm 0.02 \mu\text{eV T}^{-2}$ and $\sigma_B^* = 0.11 \pm 0.02 \mu\text{eV T}^{-2}$ were obtained for the A and B excitons, respectively. Using the theoretically estimated reduced mass of the A exciton, ranging from 0.15 to $0.22m_e$, $a_{B,A}^* = 1.48 - 1.79$ nm is obtained.

Furthermore, the exciton binding energy and wavefunction can be determined by numerically solving the 2D Schrödinger equation with the values σ and a_B determined in these measurements. For 2D TMDs, a modified Coulomb potential $U(\rho)$ was used in the calculation,

$$U(\rho) = -\frac{e^2}{8\epsilon_0\rho_0} \left[H_0\left(\frac{\rho}{\rho_0}\right) - Y_0\left(\frac{\rho}{\rho_0}\right) \right] \quad (37)$$

where H_0 and Y_0 are the Struve function and Bessel function of the second kind, respectively, and the characteristic screening length $\rho_0 = 2\pi\chi_{2D}$, where χ_{2D} is the 2D polarizability of the monolayer material. Such a potential follows a $1/\rho$ Coulomb-like potential for large electron-hole separations $\rho \gg \rho_0$, but diverges weakly as $\log(\rho)$ for small separations $\rho \ll \rho_0$, leading to a different Rydberg series of exciton states with modified wavefunctions and binding energies that cannot be described within a hydrogen-like model. By doing this, some characteristic parameters are obtained for the A and B excitons in monolayer WS_2 . For example, with $\mu_A^* = 0.16m_0$ and $a_{B,A}^* = 1.53$ nm, the binding energy of the A exciton is calculated as $E_{b,A}^* = 410$ meV. For the B exciton with $\mu_B^* = 0.27m_0$ and $a_{B,B}^* = 1.16$ nm, $E_{b,B}^* = 470$ meV.

Perovskites

Solar cells based on organic-inorganic tri-halide perovskites show significantly improved performance, and therefore, it is very important to know their fundamental optical properties, such as the exciton binding energy and the reduced mass, in order to better understand the functions of solar cells. In addition, these materials have structural phase transitions from cubic ($T > 350$ K) to tetragonal ($T > 145$ K) to orthorhombic (low T), which leads to different band structures and band gaps in the different phases. By performing transmission measurements on a ~ 300 -nm-thick polycrystalline film of $\text{CH}_3\text{NH}_3\text{PbI}_3$ in a high B up to 150 T and at different temperatures, Miyata *et al.* obtained accurate values for the exciton binding energy and reduced mass.

As shown in **Fig. 4**, at 2 K, the transition energies are observed to depend quadratically on B for the lowest two states (labeled “ $N=0$ ”), as well as the “ $N=1$ ” transition at $B < 50$ T, indicating an excitonic feature for these low-energy states. On the other hand, the transition energies depend linearly on B for the $N=1$ transition at $B > 50$ T, and the higher energy states. The authors used full numerical calculations to fit the B -dependent transition energy data and obtained an accurate value for the reduced mass $\mu^* = 0.104 \pm 0.003m_e$. They also obtained the exciton binding energy $E_b^* = 16 \pm 2$ meV, which is over three times smaller than previously assumed. At room temperature, in the tetragonal structural phase, the exciton binding energy decreases to only a few meV, due to a frequency dependent dielectric constant, which reveals the free-carrier like nature of the photovoltaic device performance at room temperature.

Quantum Wires and Dots

Similar to 2D excitons in quantum wells, 1D excitons are observed in quantum wires, showing combined effects of magnetic fields and quantum potential in high magnetic fields. Nagamune *et al.* measured photoluminescence (PL) spectra of a GaAs quantum wire in fields up to 40 T, with three orthogonal B configurations. **Fig. 5(a)** displays the PL peak position as a function of B in different configurations, for the GaAs quantum wire and a bulk GaAs sample. The bulk PL peak shifts are almost independent of the magnetic field configuration, in contrast with a clear magnetic anisotropy observed in the quantum wire sample.

In the low- B limit, the PL peaks for the quantum wire show a quadratic increase with B , from which the diamagnetic-shift coefficients were determined as $16.3 \mu\text{eV T}^{-2}$, $7.0 \mu\text{eV T}^{-2}$, and $4.5 \mu\text{eV T}^{-2}$ for the $\vec{W} \perp \vec{B} \parallel \vec{k}$, $\vec{W} \perp \vec{B} \perp \vec{k}$ and $\vec{W} \parallel \vec{B} \perp \vec{k}$ configurations, respectively, where \vec{W} is the direction along the quantum wire, and \vec{k} the wavevector of the excitation beam. These values are smaller than $103.9 \mu\text{eV T}^{-2}$ for the bulk sample, indicating increased confinement in a reduced dimensionality.

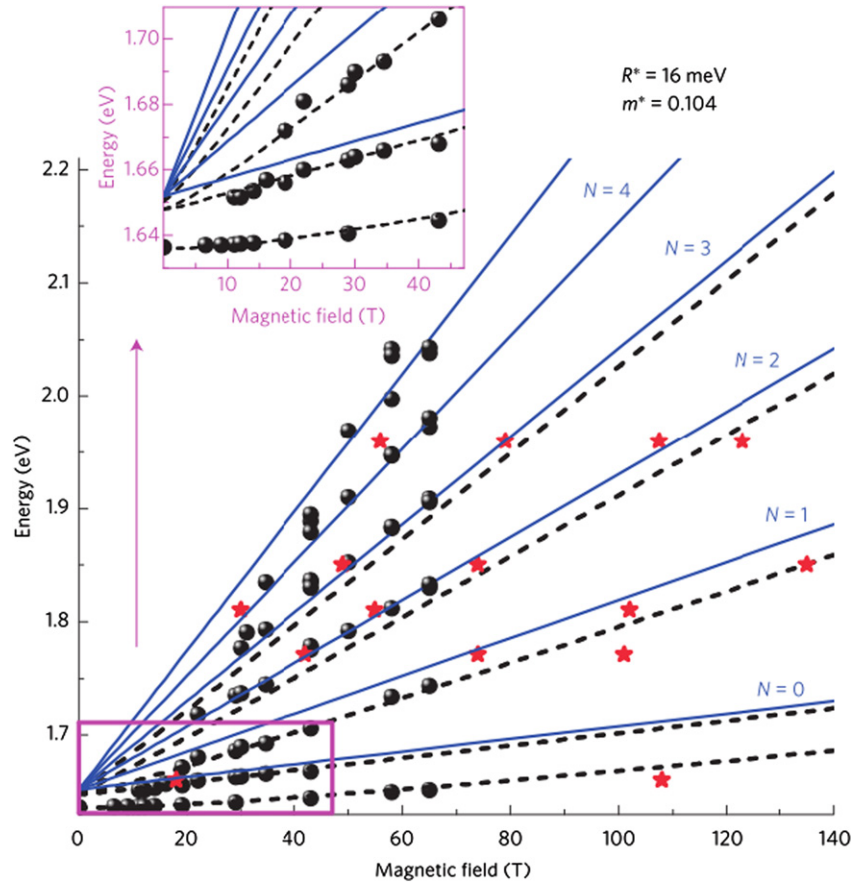


Fig. 4 (color online). Magnetic-field-dependent transition peaks of the perovskite $\text{CH}_3\text{NH}_3\text{PbI}_3$ at 2 K. The calculated transition energies are shown for the free-electron and hole levels (solid lines) and the excitonic transitions (dashed lines). Inset: measured and calculated transition energies at low fields. Reproduced (adapted) with permission from Miyata, A., Mitoglu, A., Plochocka, P., *et al.*, 2015. Direct measurement of the exciton binding energy and effective masses for charge carriers in organic-inorganic tri-halide perovskites. *Nature Physics* 11, 582–588. Copyright 2015 by Nature Publishing Group.

In the high- B limit, the PL peak shifts increase roughly linearly with increasing B . In particular, the PL energy shift under $\vec{W} \perp \vec{B} \parallel \vec{k}$ is almost parallel to that of a bulk sample, which is ascribed to the exciton radius becoming much smaller than the width of the confinement potential in a high B .

In quantum dots, electrons and holes are confined in all three directions, and quasi-zero-dimensional (0D) excitons are observed. Hayden *et al.* performed magneto-PL measurements on self-assembled InGaAs quantum dots in B up to 42 T. The PL peak shifts as a function of B are shown in Fig. 5(b) for different samples and B directions. Similar to the case of quantum wires, the low- B data is characterized by a diamagnetic shift, and the high- B data indicates a Landau-level like behavior. In addition, the diamagnetic shift is always smaller when B is applied perpendicular to the growth direction rather than parallel to it, revealing that the 0D excitons are better confined in the plane perpendicular to B .

Carbon Nanotubes

Single-wall carbon nanotubes (SWCNTs) are another representative 1D semiconductor, which are tubular crystals composed of sp^2 -bonded carbon atoms. Unlike quantum wires, the basic properties of SWCNTs are determined by a pair of integers, or chirality, (n, m) . For tubes with $n = m$, they are metals, called “armchair” tubes; for tubes with $n - m = 3j$ (j is nonzero integer), they are small-gap semiconductors; and all others are medium-gap semiconductors. In an applied B where the magnetic flux ϕ passes through the axial direction of the SWCNTs (a tube threading flux), the quantum states of electrons in SWCNTs acquire an Aharonov-Bohm phase $2\pi\phi_0/\phi_0$ ($\phi_0 = h/e$ is the magnetic flux quantum), causing the band structure of SWCNTs to change with ϕ/ϕ_0 . For $0 < \phi/\phi_0 < 1/6$, the Aharonov-Bohm phase can cause a band gap change of $6E_g\phi/\phi_0$ (E_g is the band gap) in a semiconducting SWCNT, which can be observed in interband absorption and PL measurements.

In a semiconducting SWCNT with time-reversal symmetry, at $B = 0$ T, as shown in Fig. 6(a), the bonding-like and anti-bonding-like linear combinations of two equivalent valleys, K and K' , result in two lowest energy exciton states: optically active (or “bright”) and inactive (or “dark”) states. The energies of the two states are split by Δ_X , which is determined by the Coulomb interaction, the

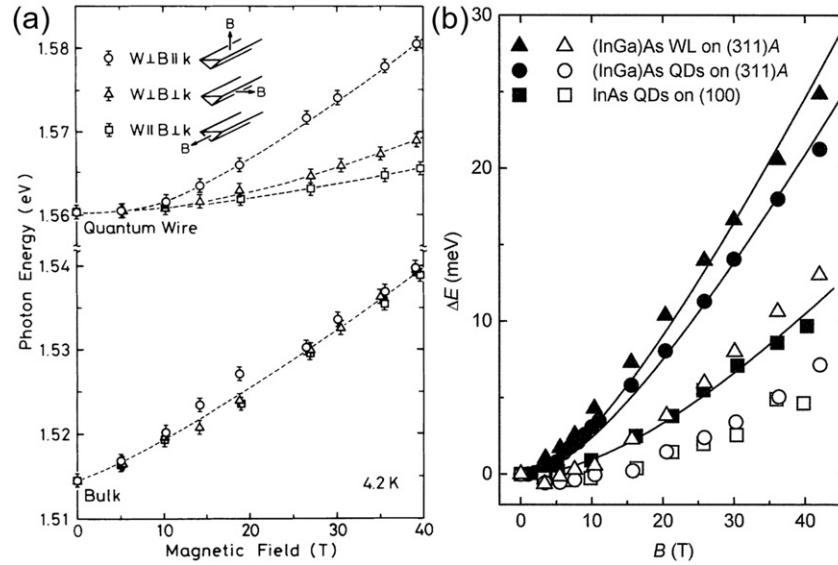


Fig. 5 (color online). (a) PL peak positions for a GaAs quantum wire and bulk GaAs samples as a function of B under various B configurations. Reproduced (adapted) with permission from Nagamune, Y., Arakawa, Y., Tsukamoto, S., Nishioka, M., 1992. Photoluminescence spectra and anisotropic energy shift of GaAs quantum wires in high magnetic fields. *Physical Review Letters* 69, 2963–2966. Copyright 1992 by the American Physical Society. (b) PL peak shifts as a function of B applied parallel to the growth axis (filled symbols) and perpendicular to the growth axis (open symbols), for quantum dots and wetting layers on different substrates. Reproduced (adapted) with permission from Hayden, R.K., Uchida, K., Miura, N., *et al.*, 1998. High field magnetoluminescence spectroscopy of self-assembled (InGa)As quantum dots on high index planes. *Physica B: Condensed Matter* 246, 93–96. Copyright 1998 by Elsevier.

tube diameter, and the dielectric constant of the environment. However, an applied B will break the time-reversal symmetry, and lift the $K-K'$ degeneracy, so that the dark state becomes optically active when the Aharonov-Bohm-induced splitting is larger than the Coulomb-induced splitting ($\Delta_{AB} > \Delta_X$). As a result, magnetic brightening of the dark exciton state can be observed in interband absorption or PL.

Fig. 6(b) shows absorption spectra of semiconducting SWCNTs at different B up to 71 T in a Voigt geometry, i.e., the light propagation vector is perpendicular to \vec{B} . The absorption increases with B , since the suspended carbon nanotubes progressively aligned with B more strongly due to the anisotropy of the magnetic susceptibility. The three main absorption peaks at $B=0$ T are labeled as A, B, and C, and each absorption peak splits into two well-resolved peaks at $B > 55$ T, due to the Aharonov-Bohm-induced splitting. This phenomenon can only be observed when the light polarization is parallel with B , as shown in **Fig. 6(c)**, as a result of magnetic anisotropy in SWCNTs.

Fig. 6(d) shows a PL contour map of a partially aligned carbon nanotube film in pulsed fields up to 56 T at 5 K. The PL intensity increases with B due to magnetic brightening. Furthermore, the Aharonov-Bohm effect causes a red-shift of each PL emission peak, since only the formerly dark state is populated due to a splitting much larger than the thermal energy. At low temperatures, the broken time-reversal symmetry increases the PL quantum yield by as much as a factor of 6, as shown in **Fig. 6(e)**. The magnetic brightening becomes weaker with increasing temperature; for instance, at 200 K the integrated PL intensity only increases by ~ 2 times.

Magnetic brightening has also been observed in single-nanotube PL. In this case, inhomogeneous broadening due to environmental effects are negligible, especially at low temperatures, and the dark-bright splitting, Δ_X , can be larger than the linewidth. Then, the dark state can become bright with an applied magnetic field. **Fig. 6(f)** shows B -dependent single-tube PL spectra at 5 K with B applied along the tube axis. At $B=0$ T, only a single, sharp PL peak can be observed, due to the bright exciton state. With increasing B , a second PL peak appears on the low energy side, grows rapidly in intensity and finally dominates the emission spectra at $B > 3$ T. The splitting between the two PL peaks increases with B . These behaviors were universally observed for more than 50 tubes of different chiralities, and the dark-bright splitting was 1–4 meV for tube diameters 1.0–1.3 nm.

Intraexciton Magneto-optical Absorption

Photoluminescence and absorption measurements can reveal information on interband transitions of s -like states of excitons. However, in order to explore the internal structure of excitons, intraexciton transitions such as $1s \rightarrow np$ ($n=2,3,\dots$) transitions have to be studied using far-infrared (FIR) or terahertz (THz) radiation, whose photon energy is comparable to or smaller than the binding energy of excitons.

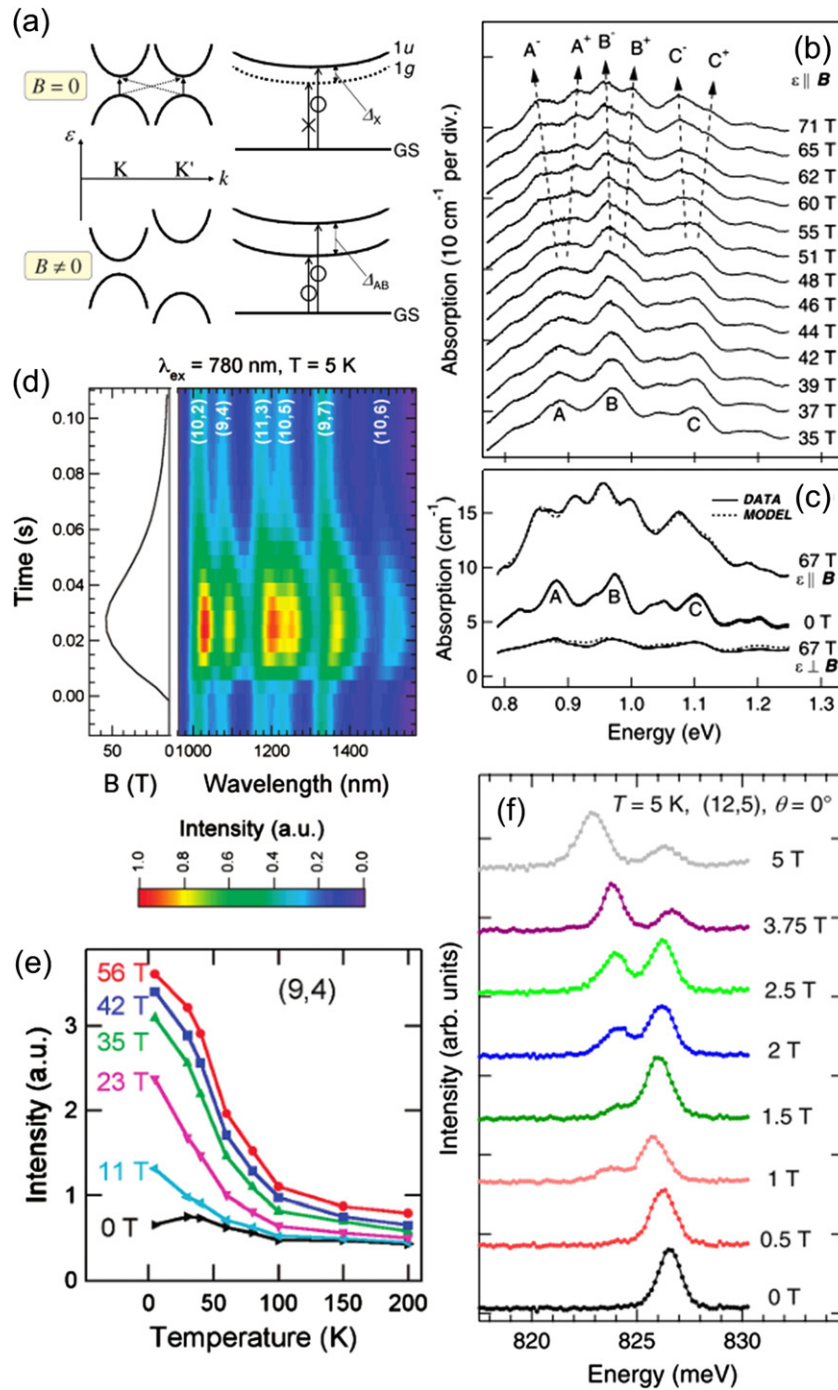


Fig. 6 (color online). (a) The expected B evolution of $K-K'$ intervalley mixing and splitting in a single-particle picture (left) and an excitonic picture (right). The solid (dashed) line represents a bright (dark) exciton state. Δ_X : Coulomb-induced splitting; Δ_{AB} : Aharonov-Bohm-induced splitting. Near band-edge absorption in semiconducting SWCNTs in high B for polarization (b) parallel to B (traces are offset) and (c) both polarizations (no intentional offset). Reproduced (adapted) with permission from Zaric, S., Ostojic, G. N., Shaver, J., *et al.*, 2006. Excitons in carbon nanotubes with broken time-reversal symmetry. *Physical Review Letters* 96, 016406. Copyright 2006 by the American Physical Society. (d) Magnetic brightening in SWCNTs in pulsed B . (e) Temperature dependence of magnetic brightening for (9,4) SWCNTs. Reproduced (adapted) with permission from Shaver, J., Kono, J., Portugall, O., *et al.*, 2007. Magnetic brightening of carbon nanotube photoluminescence through symmetry breaking. *Nano Letters* 7, 1851–1855. Copyright 2007 by the American Chemical Society. (f) B -dependent PL spectra for a single tube, showing the appearance of a dark exciton peak at a lower energy with respect to the main bright emission peak when B is applied parallel to the tube axis. Reproduced (adapted) with permission from Srivastava, A., Htoon, H., Klimov, V.I., Kono, J., 2008. Direct observation of dark excitons in individual carbon nanotubes: inhomogeneity in the exchange splitting. *Physical Review Letters* 101, 087402. Copyright 2008 by the American Physical Society.

FIR Magnetoabsorption in Photoexcited Bulk Semiconductors

Observation of intraexciton magneto-absorption in bulk semiconductors was initiated by Gershenzon *et al.* on the indirect bandgap semiconductor germanium in the microwave frequency range. Subsequently, Muro *et al.* and Ohyaama observed FIR magnetoabsorption of indirect excitons in germanium and silicon, respectively.

Fig. 7(a) shows FIR magnetoabsorption spectra for undoped germanium induced by interband photoexcitation at 4.2 K for various wavelengths. The observed spectra consist of exciton lines (E_X) and cyclotron resonance (CR) lines (C_e and C_h). Since the valence band is four-fold degenerate at the Γ point in germanium, the indirect free exciton states are described by four coupled effective mass equations, leading to the observation of four types of excitonic peaks in the spectra, E_{X1} , E_{X2} , E_{X3} , and E_{X4} . Up to the highest photoexcitation intensity used, these exciton peaks were stable against the formation of e - h droplets. The splitting of C_e' comes from the slight tilt of B from the $[100]$ -crystal axis. C_{h1} , C_{h2} , C_{h3} , and C_{h4} correspond to different cyclotron transitions related to the light-hole and heavy-hole bands.

Fig. 7(b) shows the transition energies of intraexciton lines and CR lines as a function of B . An indirect exciton in germanium is composed of an electron at the L -point and a hole at the Γ -point bound by the Coulomb interaction, giving a hydrogenic structure. At zero B , the exciton transition lines converge to a point, indicating a finite transition energy of indirect excitons, around 3 meV. At high B , where the cyclotron energy is much larger than the Coulomb interaction, the intraexciton energies are expected to increase linearly with B , although it is not observed in this experiment since the highest B (7 T) was still not large enough to satisfy the adiabatic condition (required for the decoupling of the x - y and z degrees of freedom). These results demonstrate that FIR magnetoabsorption measurements can not only reveal the CR of electrons and holes but also provide detailed information on the intraexciton transitions in indirect semiconductors with complicated band structures.

Optically Detected FIR Resonance Spectroscopy of Semiconductor Quantum Wells

In optically detected resonance (ODR) measurements, two lasers illuminate the sample at the same time. One laser with near-infrared (NIR) or visible radiation is used to create excitons, while the other with FIR (or THz) radiation manipulates them, with the frequency tuned to the resonance at a given B . By monitoring the band-edge PL, information about intraexcitonic transition energy and strength can be obtained. Fig. 8(a) shows the ratio of PL amplitudes with and without FIR irradiation as a function of B for a GaAs/AlGaAs quantum well sample, measured by Černe *et al.* Two types of transitions are observed: electron CR and the $1s \rightarrow 2p^+$ excitonic transition. At a low FIR frequency, such as 20 cm^{-1} , only electron CR can be observed at a B . With increasing FIR frequency, the electron CR shifts to a higher B , and at the same time the $1s \rightarrow 2p^+$ excitonic transition appears at a relatively low B , along with a possible $1s \rightarrow 3p^+$ excitonic transition. At a high FIR frequency, such as 130 cm^{-1} , the electron CR energy does not become equal to the FIR photon energy within the measured B range, and only excitonic transitions can be observed.

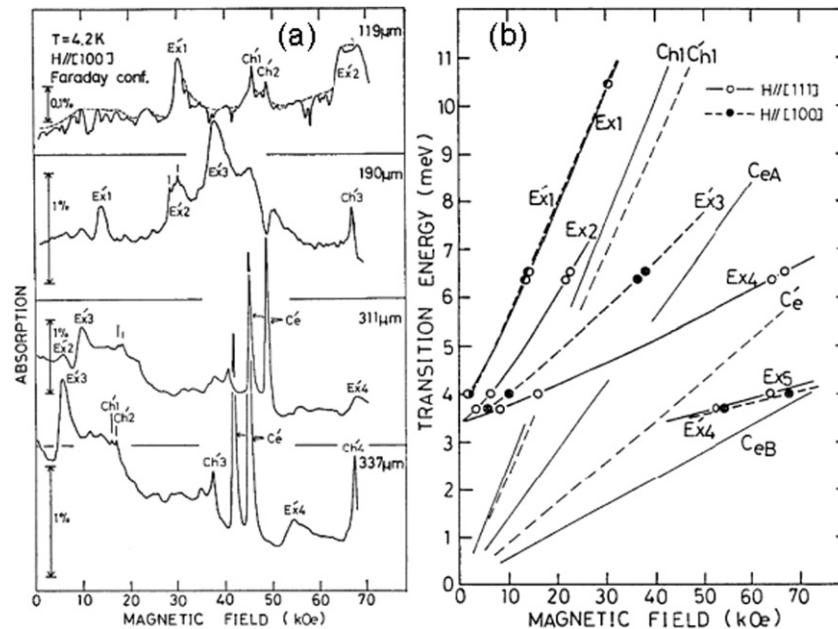


Fig. 7 (color online). (a) Magneto-absorption spectra for undoped germanium at 4.2 K with $H||[100]$ under optical excitation at varied wavelengths. (b) Transition energies of main exciton Zeeman lines and cyclotron resonance lines as a function of magnetic field. Reproduced (adapted) with permission from Muro, K., Nisida, Y., 1976. Far-infrared magneto-absorptions in photo-excited germanium. *Journal of the Physical Society of Japan* 40, 1069–1077. Copyright 1976 by the Physical Society of Japan.

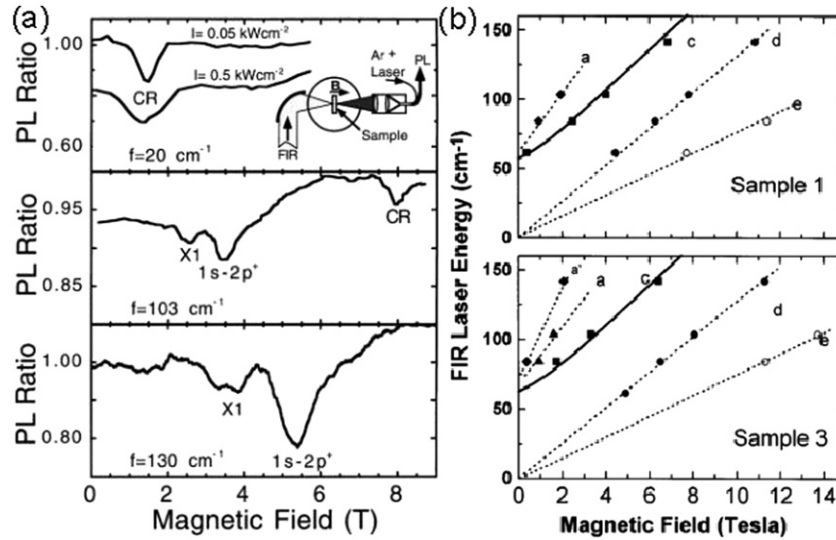


Fig. 8 (color online). Optically detected resonance spectroscopy. (a) The ratio of the PL amplitude with and without FIR irradiation as a function of B at three FIR frequencies. The inset shows the experimental setup. Reproduced (adapted) with permission from Černe, J., Kono, J., Sherwin, M. S., *et al.*, 1996. Terahertz dynamics of excitons in GaAs/AlGaAs quantum wells. *Physical Review Letters* 77, 1131–1134. Copyright 1996 by the American Physical Society. (b) Energies of the optically detected resonances as a function of B at 4.2 K. Sample 1: an undoped (12.5 nm well/15 nm barriers)₃₀ structure. Sample 3: a (8 nm well/15 nm barrier)₄₅ structure, doped with Si donors ($n = 1 \times 10^{16} \text{ cm}^{-3}$) throughout the central one-third of the wells. Reproduced (adapted) with permission from Salib, M.S., Nickel, H.A., Herold, G.S., Petrou, A., McComber, B.D., 1996. Observation of internal transitions of confined excitons in GaAs/AlGaAs quantum wells. *Physical Review Letters* 77, 1135–1138. Copyright 1996 by the American Physical Society.

Salib *et al.* also performed similar ODR measurements on GaAs/AlGaAs quantum wells to observe intraexciton transitions. **Fig. 8(b)** plots the energies of the ODR features for different quantum wells as a function of B . In both samples, electron and hole CR lines (Features d and e) are observed, with their frequencies linearly dependent on B . In addition, intraexcitonic transitions, $1s \rightarrow 2p^+$ (Feature c) and $1s \rightarrow 3p^+$ (Feature a), can also be measured. In Sample 3, even the $1s \rightarrow 4p^+$ transition (Feature a') can be well resolved. These ODR measurements provide a method to explore the internal $1s \rightarrow np$ ($n = 2, 3, \dots$) transitions of photoexcited excitons, directly determining the energies of p -like exciton states.

In the nonlinear optics version of ODR, the sample is irradiated simultaneously by a NIR beam and an intense THz beam in the presence of B . Then very strong NIR emission lines, or sidebands, appear at frequencies $\omega_{\text{NIR}} \pm 2n\omega_{\text{THz}}$, where ω_{NIR} (ω_{THz}) is the frequency of the NIR (THz) beam and n is an integer. This process is highly resonant, and thus, changes sensitively with B , providing a novel method for intraexciton spectroscopy.

Fig. 9(a) and **(b)** show typical sideband spectra at 10 T, with the THz frequency $\omega_{\text{THz}} = 115 \text{ cm}^{-1}$. **Fig. 9(a)** shows the down-conversion effect: a narrow emission line, resulting from the creation of $2s$ heavy-hole excitons, is observed at 12745 cm^{-1} , and the -2ω sideband appears at exactly $12515 \text{ cm}^{-1} [= 12745 - (2 \times 115) \text{ cm}^{-1}]$ only under the THz irradiation. **Fig. 9(b)** shows the up-conversion behavior, with $+2\omega$ and $+4\omega$ sidebands in the higher energy region, through the resonant creation of $1s$ excitons at 12531 cm^{-1} . The typical intensities of the -2ω , $+2\omega$ and $+4\omega$ sidebands are 0.05%, 0.15% and 0.0015%, respectively, of the incident intensity of the NIR excitation. The intensity of the $+2\omega$ sideband increases quadratically with the THz power under a constant NIR intensity, and increases linearly with the NIR power for a constant THz intensity. Therefore, the 2ω THz sideband generation process is a third-order nonlinear optical process, involving one NIR photon and two THz photons.

Fig. 9(c) shows the $+2\omega$ sideband intensity as a function of B with $\omega_{\text{THz}} = 115 \text{ cm}^{-1}$ and $\omega_{\text{NIR}} = \omega_{1s}$, where ω_{1s} is the frequency for $1s$ heavy-hole excitons. Three distinct resonances can be observed, located at 4.5 T, 9.5 T and 11.5 T. These resonances occur when $\omega_{\text{THz}} = \omega_{2p^+} - \omega_{1s}$, $2\omega_{\text{THz}} = \omega_{2s} - \omega_{1s}$, and $\omega_{\text{THz}} = \omega_{2p^-} - \omega_{1s}$, as shown in **Fig. 9(d)**. According to calculations using perturbation theory, the third-order nonlinear optical susceptibility $\chi^{(3)}$ is resonantly enhanced, when (A) $\omega_{\text{NIR}} = \omega_{ns}$, (B) $\omega_{\text{NIR}} + \omega_{\text{THz}} = \omega_{n'pm}$ ($m = \pm 1$), and (C) $\omega_{\text{NIR}} + 2\omega_{\text{THz}} = \omega_{n''s}$. In all three cases in **Fig. 9(d)**, two of the three conditions (A)-(C) are satisfied: (left) $\omega_{\text{NIR}} = \omega_{1s}$, $\omega_{\text{NIR}} + \omega_{\text{THz}} = \omega_{2p^+}$, (middle) $\omega_{\text{NIR}} = \omega_{1s}$, $\omega_{\text{NIR}} + 2\omega_{\text{THz}} = \omega_{2s}$, and (right) $\omega_{\text{NIR}} = \omega_{1s}$, $\omega_{\text{NIR}} + \omega_{\text{THz}} = \omega_{2p^-}$. In other words, when ω_{THz} coincides with magnetically tuned transitions of excitons, the intensity of sidebands is dramatically enhanced, which provides a highly sensitive way to explore the internal structure of excitons.

Optical-Pump/THz-Probe Magnetospectroscopy of Semiconductor Quantum Wells

In order to obtain information on the dynamics of intraexcitonic transitions, time-resolved THz spectroscopy can be a powerful technique. Zhang *et al.* performed time-resolved THz absorption measurements on photoexcited e - h pairs in undoped GaAs quantum wells at various magnetic fields, temperatures and pump intensities, investigating both CR and intraexciton resonance features through resonant and nonresonant excitations of the heavy-hole $1s$ excitons.

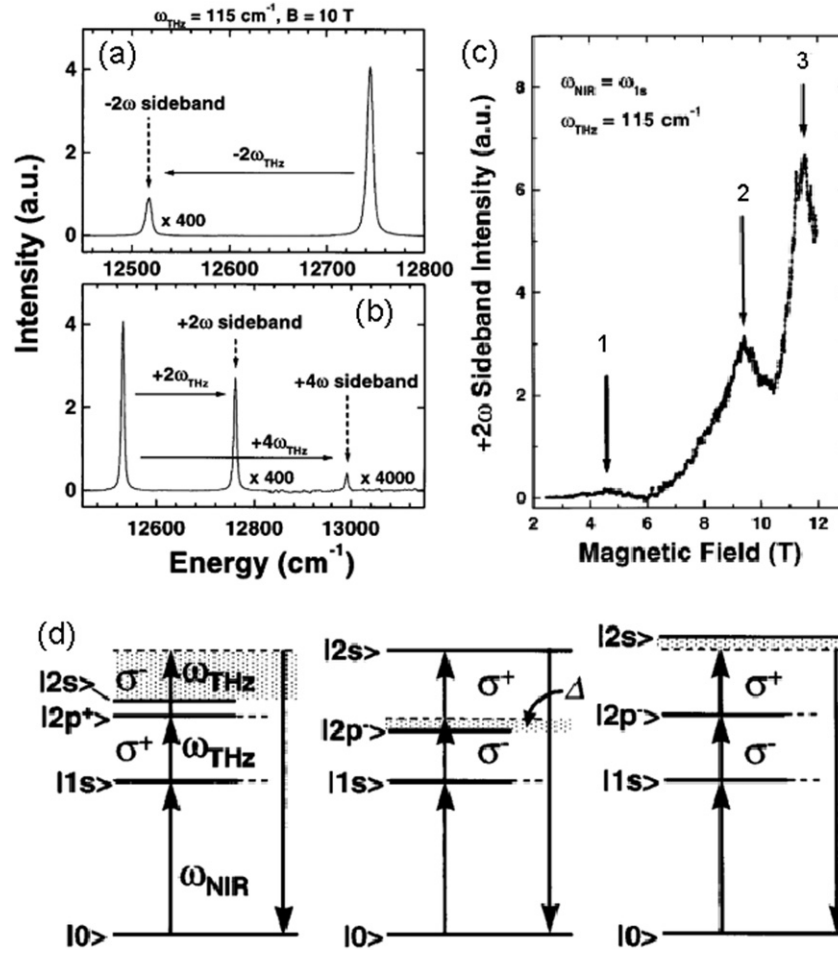


Fig. 9 (color online). Nonlinear THz ODR with $\omega_{\text{THz}} = 115 \text{ cm}^{-1}$. (a) Down conversion: $\omega_{\text{NIR}} = \omega_{2s} = 12745 \text{ cm}^{-1}$ and $\omega_{\text{sideband}} = \omega_{\text{NIR}} - 2\omega_{\text{THz}} = 12515 \text{ cm}^{-1}$. (b) Up conversion: $\omega_{\text{NIR}} = \omega_{1s} = 12515 \text{ cm}^{-1}$, $\omega_{\text{sideband}} = \omega_{\text{NIR}} + 2\omega_{\text{THz}} = 12745 \text{ cm}^{-1}$, and $\omega_{\text{NIR}} + 4\omega_{\text{THz}} = 12975 \text{ cm}^{-1}$. (c) The B dependence of the $+2\omega$ sideband intensity for $\omega_{\text{NIR}} = \omega_{1s}$ at all B . The data demonstrate nonlinear THz ODR. Pronounced resonances occur when 1: $\omega_{\text{THz}} = \omega_{2p^+} - \omega_{1s}$, 2: $2\omega_{\text{THz}} = \omega_{2s} - \omega_{1s}$, and 3: $\omega_{\text{THz}} = \omega_{2p^-} - \omega_{1s}$. (d) Diagrammatic representation of the three resonances in (c). The dashed lines represent virtual levels, whereas the solid lines represent real magnetoexcitonic levels. Resonances occur when real levels coincide with virtual levels. The shaded area represents the magnitude of the detuning, Δ . Reproduced (adapted) with permission from Kono, J., Su, M.Y., Inoshita, T., *et al.*, 1997. Resonant terahertz optical sideband generation from confined magnetoexcitons. *Physical Review Letters* 79, 1758–1761. Copyright 1997 by the American Physical Society.

Fig. 10(a) and **(b)** show the photoinduced change in conductivity, $\text{Re}\Delta\sigma(\omega)$, as a function of B and energy, at different time delays after nonresonant excitation at 5 K. At 15 ps, two distinct CR features due to unbound electrons and holes are observed, from which the effective masses can be determined: $m_e^* = 0.070m_e$ and $m_h^* = 0.54m_e$. At 1 ns, the intraexcitonic transitions, $1s \rightarrow 2p^+$ and $1s \rightarrow 2p^-$, are also observed, indicating the formation of excitons.

Fig. 10(c) and **(d)** present the time evolution of the change in conductivity at 9 T and 6 K with a pump fluence of 200 nJcm^{-2} for nonresonant and resonant excitation, respectively. Under nonresonant excitation, hole CR is observed at early time delays, such as 5 ps and 100 ps, but then decays with time and eventually the $1s \rightarrow 2p^-$ intraexciton transition appears after 100 ps. However, in the case of resonant excitation, only the $1s \rightarrow 2p^-$ transition can be observed throughout the entire time delay range, due to the direct creation of excitons. The change in conductivity gradually decreases with time through interband recombination. Through optical pump/THz-probe spectroscopy of magneto-excitons, in addition to exploring the internal structure of excitons, we are able to explore the dynamics of their formation and transitions from bound excitons to unbound electron-hole pairs.

Many-Body Effects of High-Density Excitons in High Magnetic Fields

With increasing e - h pair density, excitons can ionize to form an e - h plasma, where the electrons and holes are no longer bound to one another. This transition from excitons to an e - h plasma is referred to as the excitonic Mott transition. Here, we will focus on this high-density regime but in high B , where many-body effects can lead to many exotic behaviors, which are not observed in

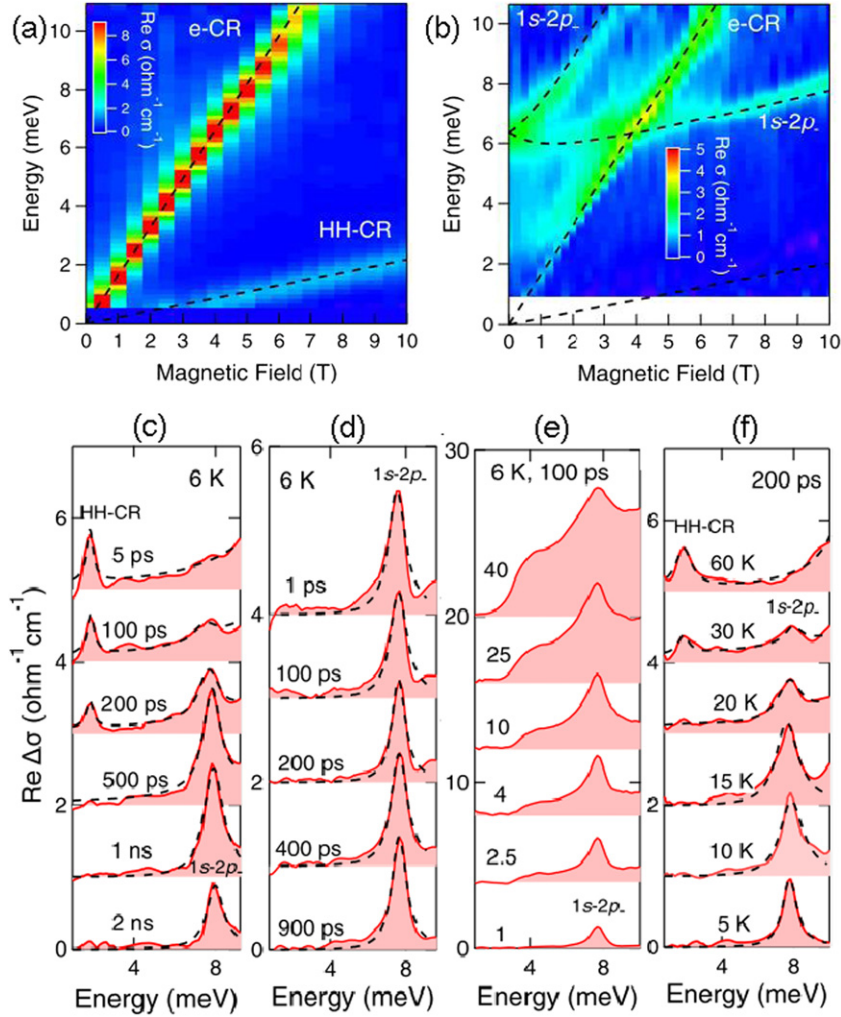


Fig. 10 (color online). Photoinduced change in conductivity, $\text{Re}\Delta\sigma(\omega)$, as a function of B , at a time delay of (a) 15 ps and (b) 1 ns after nonresonant excitation of undoped GaAs quantum wells. Conductivity spectral evolution after (c) nonresonant and (d) resonant excitations with a fluence of 200 nJcm^{-2} at 9 T. (e) Pump fluence dependent conductivity spectra at 9 T, 5 K, and 100 ps after resonant excitation. (f) Temperature-dependent conductivity spectra at 9 T and 200 ps after resonant excitation. Reproduced (adapted) with permission from Zhang, Q., Wang, Y., Gao, W., *et al.*, 2016. Stability of high-density two-dimensional excitons against a Mott transition in high magnetic fields probed by coherent terahertz spectroscopy. *Physical Review Letters* 117, 207402. Copyright 2016 by the American Physical Society.

low-density interband and intraband absorption measurements. For example, in the high-density regime of a magnetoplasma, a macroscopic coherent dipole polarization can form initially from quantum fluctuations and finally release coherent, intense superfluorescent pulses of radiation. Another interesting phenomenon that occurs in the high- B limit of 2D magnetoexcitons is that they become ultrastable against the Mott transition due to the presence of a “hidden symmetry” that cancels the interactions between excitons.

Hidden Symmetry of 2D Magnetoexcitons

The hidden symmetry is unique to 2D magnetoexcitons and can be observed under the following conditions: the Coulomb interaction is charge-symmetric, and mixing of Landau levels can be neglected. Experimentally, the hidden symmetry can be observed when the filling factors of electrons and holes satisfy $0 \leq \nu_e, \nu_h \leq 2$, i.e., only the lowest Landau level is occupied. Under these conditions, the Coulomb interaction between excitons vanishes, and the 2D magnetoexcitons become ultrastable.

One example for the existence of hidden symmetry in 2D magnetoexcitons is shown in Fig. 10(e). Under 9 T, 5 K, and 100 ps after a resonant excitation of undoped GaAs quantum wells, both the intensity and linewidth of the $1s \rightarrow 2p^-$ peak increase with the pump fluence. Under the highest pump fluence ($40 \times 200 \text{ nJcm}^{-2}$), corresponding to a pair density of 10^{11} cm^{-2} per quantum well and a filling factor of $\nu_e < 2$, the intraexcitonic feature still remains and no CR is observed. Such a pair density is almost comparable to the Mott density at 0 T, so the absence of the Mott transition does confirm that the 2D magnetoexcitons are very

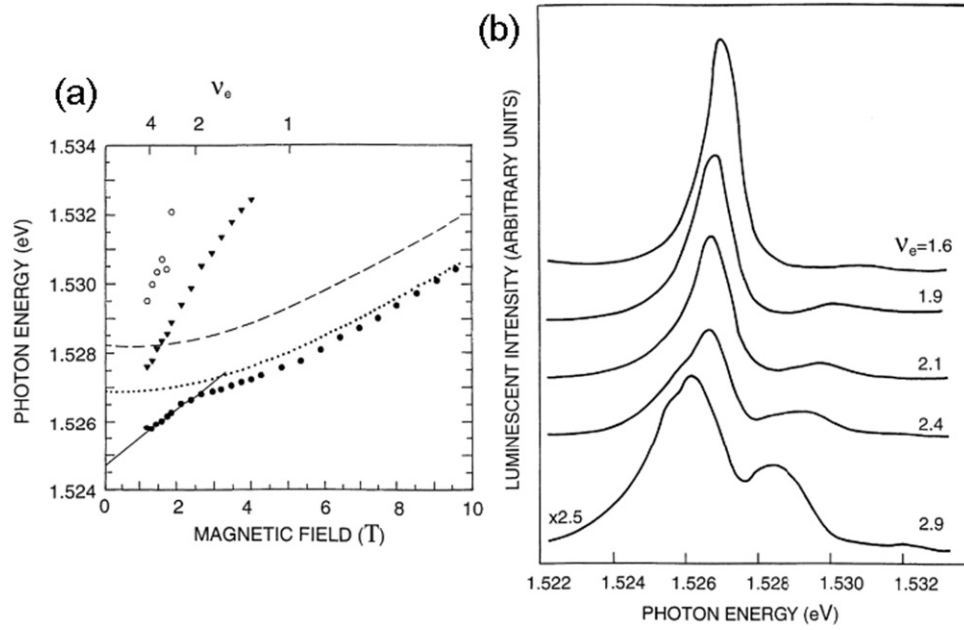


Fig. 11 (color online). (a) Photon energies of PL peak as a function of B at 4.2 K of a symmetric 20 nm quantum well with an electron density of $1.2 \times 10^{11} \text{ cm}^{-2}$. The solid line is the best fit to the linear shift of the lowest Landau level at low fields. The dashed line is the B dependence of the exciton at a low electron density, and the dotted line is that of the trion. (b) Photoluminescence spectra in the vicinity of $\nu_e = 2$. Reproduced (adapted) with permission from Rashba, E.I., Sturge, M.D., Yoon, H.W., Pfeffer, L.N., 2000. Hidden symmetry and the magnetically induced “Mott transition” in quantum wells containing an electron gas. *Solid State Communications* 114, 593–596. Copyright (2000) by Elsevier.

stable against the density-driven dissociation. However, the 2D magnetoexcitons dissociate under thermal excitation, as shown in Fig. 10(f). At a low temperature, the $1s \rightarrow 2p^-$ peak dominates the spectrum, and disappears with increasing temperature. At a high temperature, only the CR feature can be observed.

The hidden symmetry was also observed in quantum wells containing an electron gas. As shown in Fig. 11(a), at a certain B , the photon energy of the lowest transition changes from a linear dependence to a quadratic dependence on B . Above this critical B , the emission energy is very close to that of the singlet trion transition observed in the same quantum well at a low electron density. Different from a Mott transition, which is induced by the changes in screening and band-filling, this magnetically induced transition at a certain field results from the changes of the dynamic symmetry of the system, or hidden symmetry. Therefore, it is called a symmetry-driven transition.

Fig. 11(b) shows the effect of hidden symmetry in the vicinity of $\nu_e = 2$. At a relatively large filling factor for electrons, such as $\nu_e = 2.9$, the PL spectrum consists of three peaks, from the lowest Landau level transition, the blue-shifted cyclotron resonance, and a red-shifted satellite, possibly due to a phonon-assisted transition. With decreasing ν_e , the shape of the spectrum changes and the linewidth becomes sharp. That is because, under a critical B where $\nu_e < 2$, the frequency of the optical transition is not affected by the presence of electrons or holes, and the transition remains sharp.

Superfluorescence from High-Density 2D Magnetoexcitons

The concept of superradiance (SR) was proposed by Dicke in 1954, where he studied the radiative decay of an ensemble of N_{atom} incoherently excited two-level atoms, as shown in Fig. 12(a). If all of the atoms are confined in a region smaller than λ , where λ is the wavelength corresponding to the level separation, the emission behavior dramatically depends on the density of atoms. At a low density, the atoms do not interact with each other, and they radiate spontaneously with an intensity $\propto N_{\text{atom}}$ and a decay rate T_1^{-1} , where T_1 is the spontaneous radiative decay time of an isolated atom. However, at high density, all of the atoms lock in phase by photon exchange, and a giant dipole $P \sim N_{\text{atom}}d$ (d : individual atomic dipole) develops during a decay time τd . The macroscopic dipole leads to an intense coherent burst of radiation, with a decay rate $\Gamma \sim N_{\text{atom}}T_1^{-1}$, N_{atom} times faster than that of an individual atom, and a short pulse duration, $\tau_p \propto 1/N_{\text{atom}}$. Therefore, the intensity scales as $\propto N_{\text{atom}}/\tau_p \propto N_{\text{atom}}^2$, a hallmark of coherent emission.

Different from SR, where the polarization is generated by an external laser field, superfluorescence (SF) is a process in which a macroscopic polarization spontaneously develops from quantum fluctuations, which has been widely observed in atomic, molecular and solid systems. Very recently, SF was observed in InGaAs/GaAs quantum wells in quantizing B , in a setup schematically shown in Fig. 12(b). Interband transitions were studied through time-resolved PL, time-integrated PL and pump-probe spectroscopy. Since optical gain exists only for electromagnetic waves propagating along the quantum well plane, SF can be observed in the edge collection while ordinary spontaneous emission (SE) is collected in the center fiber.

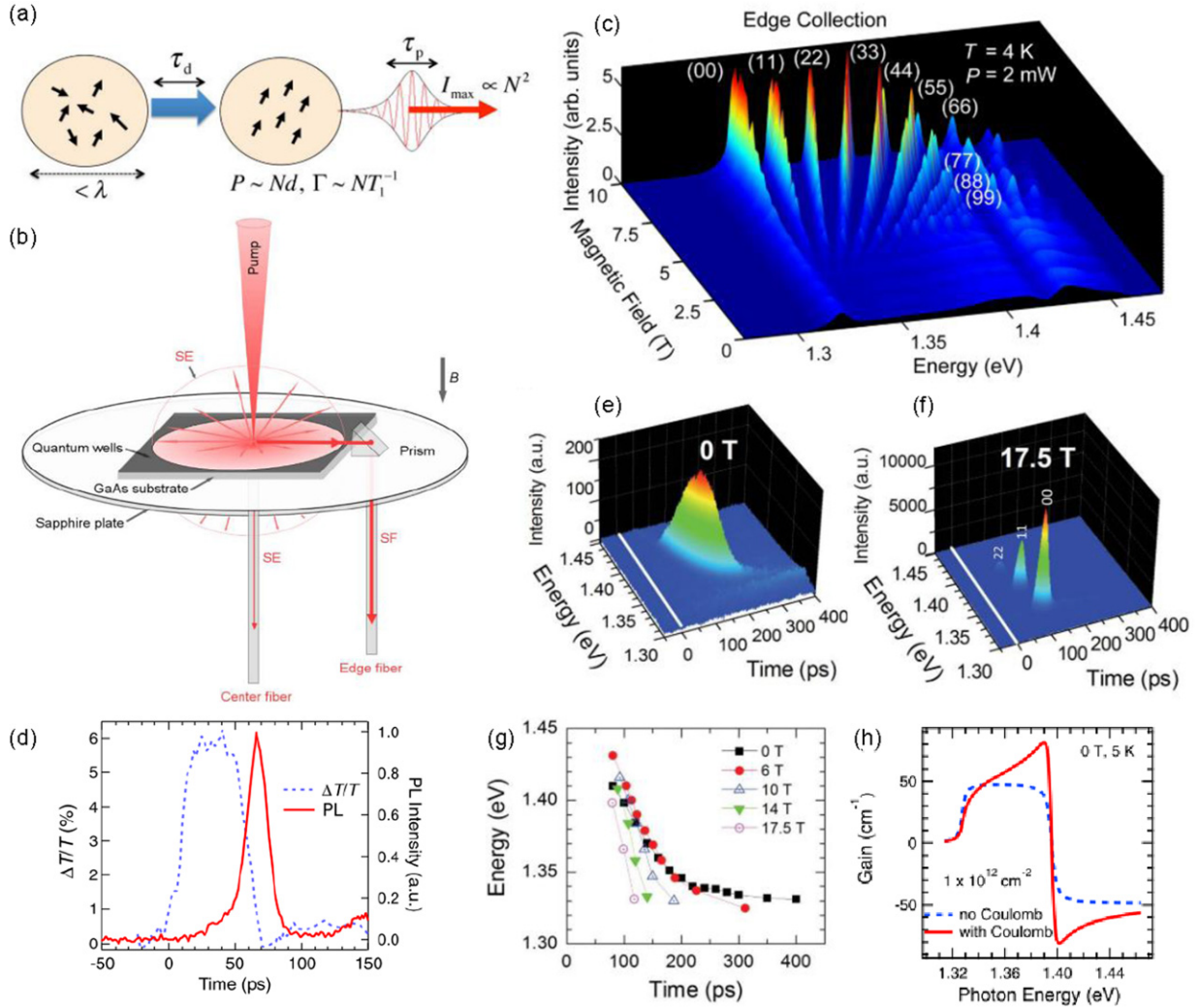


Fig. 12 (color online). (a) Basic processes and characteristics of SF. (b) Schematic diagram of the experimental geometry for SF observation from photoexcited semiconductor quantum wells in a B . (c) B dependence of time-integrated PL collected with the edge fiber at 4 K with an average excitation laser power of 2 mW. Reproduced (adapted) with permission from Cong, K., Wang, Y., Kim, J.H., *et al.*, 2015. Superfluorescence from photoexcited semiconductor quantum wells: Magnetic field, temperature, and excitation power dependence. *Physical Review B* 91, 235448. Copyright 2015 by the American Physical Society. (d) Simultaneously taken pump-probe and time-resolved PL data for the (22) transition at 17 T and 5 K, showing direct evidence of SF in the GaAs/InGaAs quantum well system. (a) and (d) reproduced (adapted) with permission from Cong, K., Zhang, Q., Wang, Y., *et al.*, 2016. Dicke superradiance in solids [Invited]. *Journal of the Optical Society of America B* 33, C80-C101. Copyright (2016) by the Optical Society of America. Time-resolved PL spectra at (e) 0 T and (f) 17.5 T with an excitation power of 2 mW at 5 K. (g) Peak shift of emission as a function of time at different magnetic fields. (h) Theoretical calculations of Coulomb-induced many-body enhancement of gain at the Fermi energy at 0 T. Reproduced (adapted) with permission from Kim, J.H., Noe II, G.T., McGill, S.A., *et al.*, 2013. Fermi-edge superfluorescence from a quantum-degenerate electron-hole gas. *Scientific Reports* 3, 3283. Copyright (2013) by Nature Publishing Group.

Fig. 12(c) shows B -dependent time-integrated SF emission at a pump intensity of 2 mW and a temperature of 4 K. At a low B (< 4 T), SF is characterized by two peaks at around 1.32 eV and 1.43 eV, corresponding to the heavy-hole and light-hole transitions, respectively. With increasing B , emission peaks due to the $(N, M) = (00), (11), \dots$, heavy-hole transitions, are observed, with stronger intensities and narrower widths.

In order to obtain direct evidence for SF emission, time-resolved pump-probe and PL measurements were performed. **Fig. 12(d)** shows pump-probe differential transmission and time-resolved PL data for the (22) transition at 17 T and 5 K. The pump creates the population inversion, as seen from the differential transmission, but at a time delay around 70 ps, it suddenly drops to zero, and at the same time a strong pulse of emission appears, as indicated by the time-resolved PL data.

The SF emission at 0 T is characterized by a continuous burst after a certain time delay, as shown in **Fig. 12(e)**, while the effects of quantization are obvious at a high B , as seen in **Fig. 12(f)**. By analyzing the emission time for different energies at various magnetic fields, as shown in **Fig. 12(g)**, a sequential manner of SF emission is found: SF from the highest occupied states is emitted

first, which is followed by emission from lower energy states. In addition, it can be seen that the SF emission occurs at shorter delay times with increasing B .

These results can be explained by the excitonic enhancement of gain near the Fermi energy in a high-density electron-hole system, as shown in Fig. 12(h). After relaxation and thermalization, degenerate Fermi gases form inside the conduction and valence bands each with quasi-Fermi energies. The recombination gain just below the quasi-Fermi energy is enhanced due to Coulomb interactions among carriers, which causes a SF burst to form at the Fermi edge. After the SF emission, the population is depleted, leading to a decreased Fermi energy. Thus, as time progresses, the Fermi level moves toward the band edge continuously. As a result, a continuous SF emission is observed at zero field and a series of sequential SF bursts appear in a magnetic field.

Summary

In this review, we have shown that the presence of excitons significantly modifies the optical response of semiconductor materials. Magneto-optical spectroscopy provides a powerful experimental means to determine the basic parameters of excitons such as the reduced mass, binding energy, Bohr radius, g -factor, internal structure, and formation dynamics. Depending on the dimensionality of excitons, these parameters can vary greatly, and we have presented experimental observations in magnetic fields for varied systems, including bulk semiconductors, 2D semiconductor quantum wells, monolayer TMDs, 1D quantum wires, SWCNTs, and semiconductor quantum dots. In addition to characterizing exciton parameters, magneto-optical spectroscopy of semiconductors can reveal exotic phenomena such as the "hidden symmetry" of 2D excitons in high magnetic fields and superfluorescence from a semiconductor magnetoplasma. The powerful experimental tools we have discussed will surely continue to reveal new phenomena related to excitons in semiconductors, including intriguing features related to the bosonic nature of excitons.

Further Reading

- Akimoto, O., Hasegawa, H., 1967. Interband optical transitions in extremely anisotropic semiconductors. II. Coexistence of exciton and the Landau levels. *Journal of the Physical Society of Japan* 22, 181–191.
- Černe, J., Kono, J., Sherwin, M.S., *et al.*, 1996. Terahertz dynamics of excitons in GaAs/AlGaAs quantum wells. *Physical Review Letters* 77, 1131–1134.
- Cong, K., Wang, Y., Kim, J.H., *et al.*, 2015. Superfluorescence from photoexcited semiconductor quantum wells: magnetic field, temperature, and excitation power dependence. *Physical Review B* 91, 235448.
- Cong, K., Zhang, Q., Wang, Y., *et al.*, 2016. Dicke superradiance in solids [Invited]. *Journal of the Optical Society of America B* 33, C80–C101.
- Hayden, R.K., Uchida, K., Miura, N., *et al.*, 1998. High field magnetoluminescence spectroscopy of self-assembled (InGa)As quantum dots on high index planes. *Physica B: Condensed Matter* 246, 93–96.
- Kim, J.H., Noe II, G.T., McGill, S.A., *et al.*, 2013. Fermi-edge superfluorescence from a quantum-degenerate electron-hole gas. *Scientific Reports* 3, 3283.
- Kono, J., Su, M.Y., Inoshita, T., *et al.*, 1997. Resonant terahertz optical sideband generation from confined magnetoexcitons. *Physical Review Letters* 79, 1758–1761.
- MacDonald, A.H., Ritchie, D.S., 1986. Hydrogenic energy levels in two dimensions at arbitrary magnetic fields. *Physical Review B* 33, 8336–8344.
- Miyata, A., Mitioglu, A., Plochocka, P., *et al.*, 2015. Direct measurement of the exciton binding energy and effective masses for charge carriers in organic-inorganic tri-halide perovskites. *Nature Physics* 11, 582–588.
- Muro, K., Nisida, Y., 1976. Far-infrared magneto-absorptions in photo-excited germanium. *Journal of the Physical Society of Japan* 40, 1069–1077.
- Nagamune, Y., Arakawa, Y., Tsukamoto, S., Nishioka, M., 1992. Photoluminescence spectra and anisotropic energy shift of GaAs quantum wires in high magnetic fields. *Physical Review Letters* 69, 2963–2966.
- Rashba, E.I., Sturge, M.D., Yoon, H.W., Pfeffer, L.N., 2000. Hidden symmetry and the magnetically induced "Mott transition" in quantum wells containing an electron gas. *Solid State Communications* 114, 593–596.
- Salib, M.S., Nickel, H.A., Herold, G.S., Petrou, A., McComber, B.D., 1996. Observation of internal transitions of confined excitons in GaAs/AlGaAs quantum wells. *Physical Review Letters* 77, 1135–1138.
- Shaver, J., Kono, J., Portugall, O., *et al.*, 2007. Magnetic brightening of carbon nanotube photoluminescence through symmetry breaking. *Nano Letters* 7, 1851–1855.
- Srivastava, A., Htoon, H., Klimov, V.I., Kono, J., 2008. Direct observation of dark excitons in individual carbon nanotubes: inhomogeneity in the exchange splitting. *Physical Review Letters* 101, 087402.
- Stier, A.V., McCreary, K.M., Jonker, B.T., Kono, J., Crooker, S., 2016. Exciton diamagnetic shifts and valley Zeeman effects in monolayer WS₂ and MoS₂ to 65 Tesla. *Nature Communications* 7, 10643.
- Tarucha, S., Okamoto, H., Iwasa, Y., Miura, N., 1984. Exciton binding energy in GaAs quantum wells deduced from magneto-optical absorption measurement. *Solid State Communications* 52, 815–819.
- Zaric, S., Ostojic, G.N., Shaver, J., *et al.*, 2006. Excitons in carbon nanotubes with broken time-reversal symmetry. *Physical Review Letters* 96, 016406.
- Zhang, Q., Wang, Y., Gao, W., *et al.*, 2016. Stability of high-density two-dimensional excitons against a Mott transition in high magnetic fields probed by coherent terahertz spectroscopy. *Physical Review Letters* 117, 207402.